AD_____

GRANT NUMBER DAMD17-97-1-7166

TITLE: Measurements of X-Ray Capillary Optics for Digital Mammography

PRINCIPAL INVESTIGATOR: Sushil D. Padiyar

CONTRACTING ORGANIZATION: State University of New York
Albany, New York 12222

REPORT DATE: September 1998

TYPE OF REPORT: Annual

PREPARED FOR: U.S. Army Medical Research and Materiel Command
Fort Detrick, Maryland 21702-5012

DISTRIBUTION STATEMENT: Approved for public release;
distribution unlimited

The views, opinions and/or findings contained in this report are
those of the author(s) and should not be construed as an official
Department of the Army position, policy or decision unless so
designated by other documentation.

19990713 132

REPORT DOCUMENTATION PAGE

Form Approved
OMB No. 0704-0188

1. AGENCY USE ONLY *(Leave blank)*	2. REPORT DATE September 1998	3. REPORT TYPE AND DATES COVERED Annual (1 Sep 97 - 31 Aug 98)

4. TITLE AND SUBTITLE

Measurements of X-Ray Capillary Optics for Digital Mammography

5. FUNDING NUMBERS

DAMD17-97-1-7166

6. AUTHOR(S)

Padiyar, Sushil D.

7. PERFORMING ORGANIZATION NAME(S) AND ADDRESS(ES)

State University of New York
Albany, New York 12222

8. PERFORMING ORGANIZATION REPORT NUMBER

9. SPONSORING / MONITORING AGENCY NAME(S) AND ADDRESS(ES)

U.S. Army Medical Research and Materiel Command
Fort Detrick, Maryland 21702-5012

10. SPONSORING / MONITORING AGENCY REPORT NUMBER

11. SUPPLEMENTARY NOTES

12a. DISTRIBUTION / AVAILABILITY STATEMENT

Approved for public release; distribution unlimited

12b. DISTRIBUTION CODE

13. ABSTRACT *(Maximum 200 words)*

X-ray capillary optics present great potential in designing a mammographic imaging system with high resolution, enhanced contrast, a high dynamic range and a low absorbed dose to the patient. Well engineered optics can collimate, focus and filter x-rays and can magnify images or demagnify images to mate them to a direct x-ray detector.

Measurements on two collimating prototypes as pre-patient optics and two linearly tapered optics as post-patient "scatter-rejection" devices are reported here. Preliminary scatter fraction measurements demonstrate an excellent ability to reject Compton scattered photons, implying enhanced contrast in medical imaging systems.

14. SUBJECT TERMS Breast Cancer X-ray capillary optics, Digital Mammography, early detection, Breast Cancer	15. NUMBER OF PAGES 29
	16. PRICE CODE

17. SECURITY CLASSIFICATION OF REPORT Unclassified	18. SECURITY CLASSIFICATION OF THIS PAGE Unclassified	19. SECURITY CLASSIFICATION OF ABSTRACT Unclassified	20. LIMITATION OF ABSTRACT Unlimited

FOREWORD

Opinions, interpretations, conclusions and recommendations are those of the author and are not necessarily endorsed by the U.S. Army.

_____ Where copyrighted material is quoted, permission has been obtained to use such material.

_____ Where material from documents designated for limited distribution is quoted, permission has been obtained to use the material.

_____ Citations of commercial organizations and trade names in this report do not constitute an official Department of Army endorsement or approval of the products or services of these organizations.

_____ In conducting research using animals, the investigator(s) adhered to the "Guide for the Care and Use of Laboratory Animals," prepared by the Committee on Care and Use of Laboratory Animals of the Institute of Laboratory Resources, National Research Council (NIH Publication No. 86-23, Revised 1985).

_____ For the protection of human subjects, the investigator(s) adhered to policies of applicable Federal Law 45 CFR 46.

_____ In conducting research utilizing recombinant DNA technology, the investigator(s) adhered to current guidelines promulgated by the National Institutes of Health.

_____ In the conduct of research utilizing recombinant DNA, the investigator(s) adhered to the NIH Guidelines for Research Involving Recombinant DNA Molecules.

_____ In the conduct of research involving hazardous organisms, the investigator(s) adhered to the CDC-NIH Guide for Biosafety in Microbiological and Biomedical Laboratories.

PI - Signature   29th Sept 1998
                                         Date

Table of Contents

Section I

Introduction

Results of extensive mammography screenings have shown the need for detection of breast cancer at earlier and more curable stages to have any significant impact on the mortality rate. While new imaging technologies for breast cancer diagnosis like magnetic resonance imaging, breast ultrasound and breast specific positron emission tomography are being developed, x-ray imaging continues to function as a convenient and economical choice for early detection.

A mammographic imaging system is characterized by four crucial parameters: contrast, resolution, absorbed dose to the patient and dynamic range[1]. The differences in the linear attenuation coefficient between carcinoma and normal breast parenchyma are marginal and contrast becomes highly important to detect small differences in soft tissue density. Resolution, which is a measure of the smallest lesion that the imaging system can detect, needs to be high to detect the details of microcalcifications. A small absorbed dose to the breast while maintaining a high image quality reduces the risk of radiation induced carcinogenesis. Dynamic range, which is defined as the ratio of the largest signal at detector saturation to that of the smallest signal detectable above the intrinsic noise level of the detector, needs to be high to incorporate the variation in x-ray transmission over the area of the mammogram.

Purpose

X-ray capillary optics coupled efficiently to a direct digital x-ray detector provide the basis for such a system[2]. One of the promising and exciting new detectors in consideration is based on a x-ray photoconductor, such as amorphous selenium (a semiconductor with atomic number 34), combined with an active matrix array to create a wide area flat panel image detector[3],[4]. This particular detector would convert the x-ray image directly into a digital signal for display, processing and storage.

5

X-ray capillary optics have a small angular acceptance and do not transmit high angle Compton scattered photons, thereby enhancing image contrast. Loss of resolution commonly encountered in conventional mammography (the geometric blur due to the finite source spot size) is prevented by the use of these optics as they guide the photons along individual fibers and prevent overlap of the beam emerging from spatially close areas. Enhanced contrast and higher resolution consequently, require the patient to be subjected to the same quality x-ray beam for a shorter period of time, thereby reducing the dose. Finally, such a system is amenable to mating with a digital detector, allowing computer assisted analysis of images and providing a high dynamic range.

1.1 X-ray capillary optics

X-rays had created their own niche in the medical industry within a decade of their discovery by Wilhemn Roentgen in 1895[5]. The technology of generating and harnessing x-ray beams to tap their potential in fields like material physics, medicine and protein crystallography have drawn the attention of physicists for a long time. The effort has resulted in sources of intense radiation like third generation synchrotrons and devices to control and manipulate x-rays.

While most other optics for x-rays suffer from narrow angular and spectral selectivity, x-ray capillary optics present unique advantages.
Well-engineered optics can collimate, focus and filter x-rays[6],[7] and can magnify images or demagnify images to mate them to a direct x-ray detector.

The Fresnel equations, which give the reflectivity at the interface between two dielectrics, and Snell's law[8] point to the existence of a critical angle of incidence below which all radiation is reflected back into the medium from which it is incident. This phenomenon of total reflection (also being exploited in fiber optical devices, which have revolutionized the field of optoelectronics) forms the working principle of x-ray capillary optics with air and borosilicate glass

$\left(Si_{22}O_{62}B_{10}Na_3Al_3K_1 \right)$ forming the two dielectric media.

1.2 Theory

The complex index of refraction (n) for x-rays is expressed as[9]

n = 1-δ-iβ ……………………………………… …….. (1)   with

$$\delta = \frac{\theta_c^2}{2} \text{ and } \beta = \frac{\lambda \mu}{4\pi} \quad \text{……………………………………… (2)}$$

where θ_c is the critical glancing angle for total reflection, λ is the wavelength of the incident x-rays and μ is the mass attenuation coefficient of the material and depends on the incident energy. When λ is much shorter than the critical absorption wavelength of electrons then the electrons can be considered as free electrons and δ is given by

$$\delta = \frac{Nq^2\lambda^2}{2\pi mc^2} \quad \text{……………………………………… (3)}$$

where N is the number of free electrons per unit volume, q is the electric charge, m is the electronic mass and c is the velocity of light.

The reflection coefficient which is the ratio of the intensity of reflected radiation (I_r) to the intensity of incident radiation (I_o) is obtained from the Fresnel equations and is expressed as

$$\frac{I_r}{I_0} = \left| \frac{Sin\ \theta - (\varepsilon - 1 + Sin^2\theta)^{\frac{1}{2}}}{Sin\ \theta + (\varepsilon - 1 + Sin^2\theta)^{\frac{1}{2}}} \right| \quad \text{…………………………(4)}$$

where θ is the glancing angle of the incident x rays and ε is the complex dielectric constant of the material given by n^2 .

The β/δ dependency of $\dfrac{I_r}{I_o}$ is shown in *fig 1* as a function of θ/θ_c
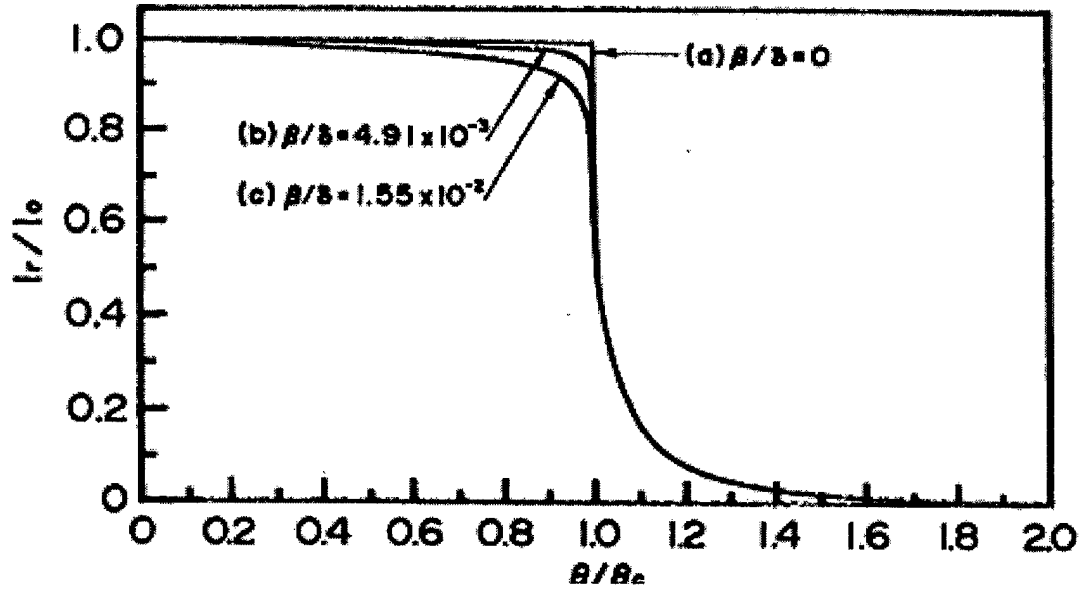

Fig 1 :   *Theoretical reflection coefficients* $\dfrac{I_r}{I_o}$ *for the selected* β/δ *as a function*

of θ/θ_c *. The curve (a) is for* β/δ *= 0   (b) is for* β/δ *= 4.91E-3 at Mo-Kβ*

and (c) is for β/δ *= 1.55E-2 at Cu-Kα.*

This figure affirms a fast drop in reflectivity at angles greater then the critical
angle. It is precisely this property of capillary optics that is beneficial in
appropriately designing a scatter rejection device to be employed in imaging
systems. Such a scatter rejection optic would enhance contrast, normally
diminished due to compton scattered photons reaching the detector plane.

X-ray Capillary optics are made up of many capillary fibers, each fiber being
made up of thousands of smooth walled channels, as shown in figure 2.
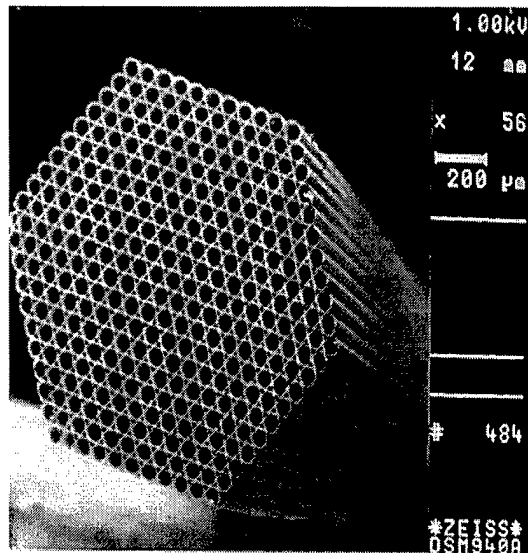
Fig 2: A typical micrograph of a polycapillary fiber with channel sizes ~ 50 microns. State of the art manufacturing technology allows adequate control over channel sizes as small as 3-5 microns.

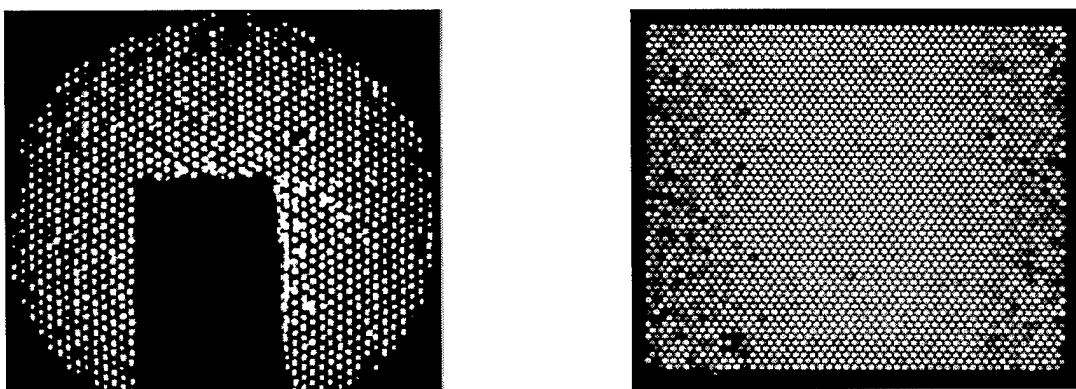## Section II
Multi-fiber Collimating optics

Multi-fiber collimating X-ray optics are manufactured by meticulously stringing capillary fibers through metal grids and are designed to collect over a large solid angle from a conventional electron bombardment laboratory source. These optics direct the beam along the capillary channels to produce a quasi-parallel x-ray field.

Two prototype multi-fiber collimating optics, the dimensions of which are presented in table I, were measured for this project.

Table I.

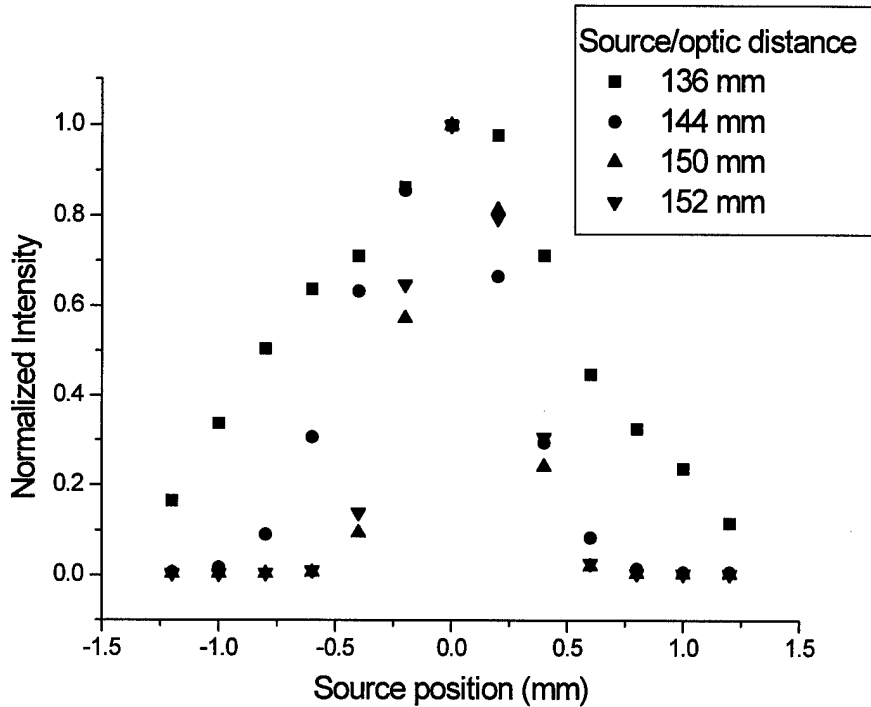| Prototype Collimating optic I	Prototype Collimating optic II
Input diameter = 23 mm	Input dimension = 28 mm
Output diameter = 35 mm	Output dimension = 30 mm
X-ray field shape: circular with 35-mm diameter.	X-ray field shape: Square with each side 30 mm.
Channel size = 17 microns.	Channel size = 10 microns.
Focal distance = 150 mm	Focal distance = 1000 mm
Transmission at Mo characteristic lines = 5 %.	Transmission at Mo characteristic lines = 35 %.

The x-ray source used in the measurements listed in tables I and II used a Molybdenum anode with characteristic lines K α and K β at 17.5 keV and 19.6 keV, respectively. A high purity Germanium detector was used to collect the spectra.

Fig 3: The X-ray fields at the output of the two collimating prototypes, I (left) and II (right).

10

A small rectangular cross-section of the prototype I (17 X 11 mm) was blocked by lead as shown in figure 3. This part of the optic had been subjected to the white beam at the National Synchrotron Light Source (NSLS) at the Brookhaven National Laboratory (BNL) to study radiation damage effects. The lead block was taken into account while calculating the transmission efficiency of the optic.

The focal distance of the optic is the distance between the input end of the optic and the source when the maximum cross-section of the optic transmits. A very reliable way to determine the focal distance is source scans that are carried out in a direction transverse to the optic axis as shown in figure 4. The widths (FWHM) of these transverse source scans are a minimum at the focal distance due to the small angular acceptance of the outer fibers in the optic.

Fig 4: Source scans transverse to the optic axis for prototype collimating optic I at different source optic distances. The source scan is the narrowest at the focal distance, i.e. 150 mm in this case.

The focal distances and the dimensions of these optics enable us to determine the acceptance cone angles of these optics as ~ 9 and 2 degrees for the prototype Collimating Optics I and II respectively.

Transmission (T) is defined as the ratio of the flux at the output of the optic to the flux incident on the optic input cross-section. Transmission measurements are performed by collecting the x-ray spectrum through a well aligned optic and then through a small pinhole. (The pinhole is typically smaller than the input diameter of the optic, to avoid dead time losses that can occur due to saturation of the detector). The ratio of the count rate with and without the optic (through the pinhole) gives the transmission. A solid angle correction is applied to this calculation to account for the difference in solid angles subtended by the optic and the pinhole at the source.

$$T = \frac{N_{optic}(E)}{N_{pinhole}(E)} * \frac{\Omega_{pinhole}}{\Omega_{optic}} \quad \dots\dots\dots\dots\dots\dots\dots\dots\dots\dots\dots\dots\dots\dots\dots\dots (5)$$

Where

$N_{optic}(E)$ is the flux at the output of the optic in the relevant energy window.

$N_{pinhole}(E)$ is the flux through a small pinhole in the same energy range.

$\Omega_{pinhole}$ is the solid angle subtended by the pinhole at the source and

Ω_{optic} is the solid angle subtended by the optic at the source.

Equation (5) in the case of an optic with a circular cross-section (prototype I) is

expressed as $\quad T = \dfrac{N_{optic}(E)}{N_{pinhole}(E)} * \left(\dfrac{D_{pinhole}}{L_{ps}} * \dfrac{L_{sl}}{D_{optic}} \right)^{2} \quad \dots\dots\dots\dots (6)$

$D_{pinhole}$, D_{optic} , L_{sl} and L_{ps} being the pinhole diameter, the optic input diameter , the source lens distance and the pinhole-source distance respectively. The results of transmission measurements carried out on the two prototypes are shown in figure 5. The prototype II transmits much better than the earlier prototype in the mammographic energy range due to better alignment of fibers in the grid.
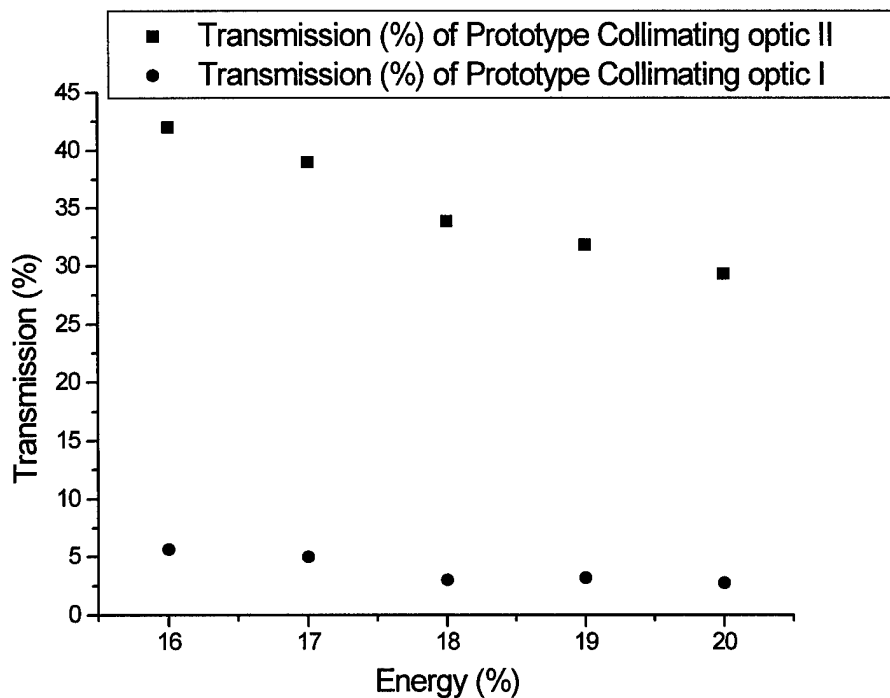
Fig 5: Transmission Vs Energy for prototype collimating optics I & II.

The beam emerging from the optic is quasi-parallel in the sense that the fibers are parallel at the output. This alleviates the problem of penumbral shadowing and also one of unequal magnification of objects at the entry and exit side of the patient. However, there is local divergence, the divergence of the beam emerging from each individual channel, which depends upon the energy of the radiation. Divergence is a very important parameter because it produces geometric blur in the image and has a profound effect on the system resolution. The local divergence from the individual channels has a value between once and twice the critical angle, for fibers that are well aligned.
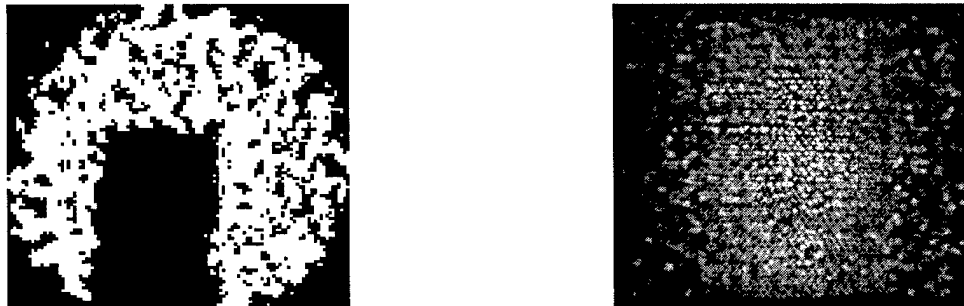
Fig 6: X-ray fields at 30 cms from output of the prototype optics I (left) and II (right). (The blur is a cause for concern for resolution properties).

This divergence can be seen in comparing figures 3 and 6. In figure 6, which was taken further from the optic, the divergence from the channels has blurred the channel walls.

The exit angle divergence of an optic can be determined by Bragg reflecting the output beam off a (100) oriented high quality silicon crystal. Since the crystal diffracts only for a very narrow angular range, rotating the crystal yields the divergence directly, as shown in figure 7.
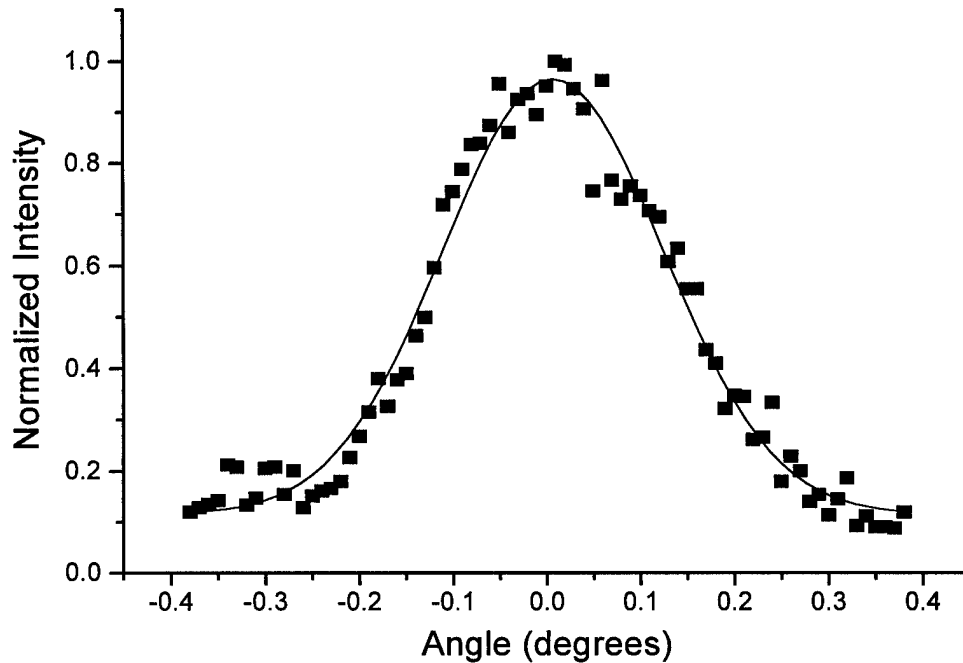
Fig 7: Output divergence measurement of the prototype collimating optic I. Intensity is plotted versus the rotation angle of the crystal.

2.1 Diffraction Gain

The term defined as "gain"[10] here refers to the increase in the diffracted beam intensity obtained by carrying out an diffraction experiment using a collimating optic in comparison with the same process carried out through a pinhole collimator having the same output divergence as the output divergence of the optic.

The prototype collimator I with an output divergence of 4.8 mrad at 17.5 keV (the Mo Kα line) yields a gain of **18** in comparison with pinhole collimated diffraction.
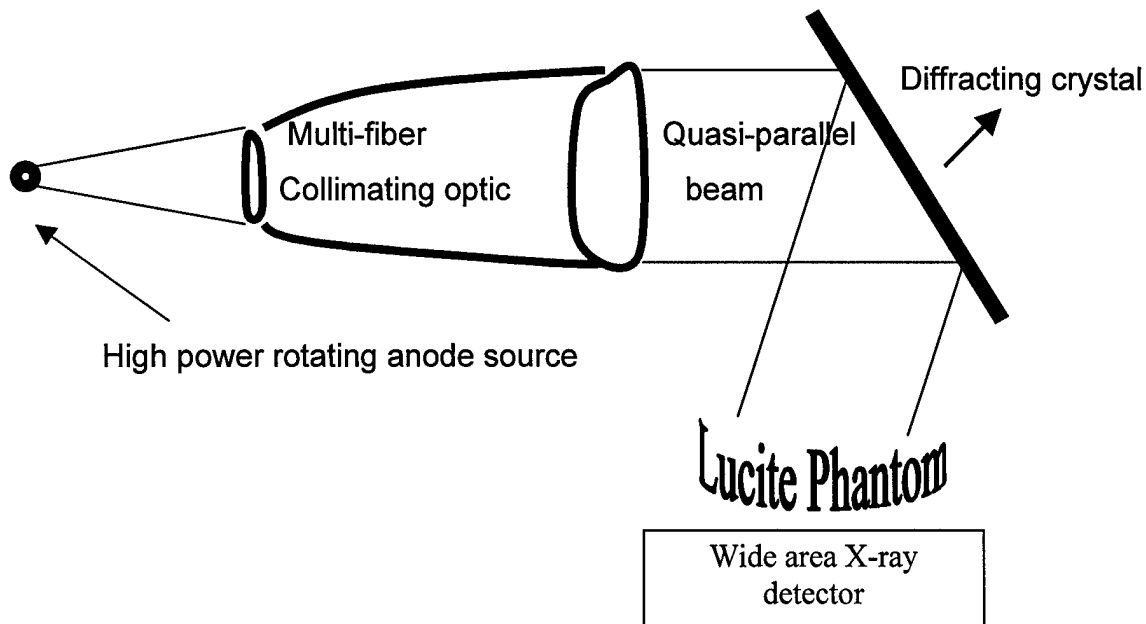
Fig 8: Set-up for monochromatic X-ray imaging experiment. The quasi-parallel output from a Multi-Fiber X-ray Collimating Optic is diffracted off a high mosaicity crystal to obtain a sufficiently intense and parallel monochromatic beam.

2.2 Monochromatic Imaging

High diffracted beam intensities are desired to produce intense and parallel monochromatic beams[11] as such beams lead to increased resolution and enhanced contrast. The "diffraction gain" described above has interesting connotations as higher diffracted beam intensities can be obtained from an optic with a low output divergence and well aligned fibers.

Contrast between carcinoma and breast parenchyma that is usually diminished due to the small differences in linear attenuation coefficient can be significantly enhanced by the use of monochromatic beams[12,13]. In addition, the distance between the patient and the source becomes irrelevant due to the parallel nature

of the diagnostic beam. This parallel beam renders possible an adequately large air gap to avoid Compton scattered photons at the detector plane.

The problems inherent in a divergent beam (from a finite source spot) are simply not encountered. Fig 8 demonstrates the schematic for such an experiment.

There is a tradeoff between contrast and absorption[14] and experiments have shown that monochromatic beams in the 17-20 keV energy range can be considered as ideal probes for the early detection of breast cancer[15],[16].

Presented below is a feasibility analysis for acquiring such monoenergetic beams by using a high power rotating anode source in conjunction with the prototype collimating optic II, which transmits close to 60 % at the copper characteristic K α line (8.5 keV). While this calculation is based on the Cu characteristic line, because of the availability of a high power Cu source in house, it is relatively straightforward to extrapolate it to energy ranges desired for mammography. The output of the collimating optic that is quasi-parallel and polychromatic can be made parallel and monochromatic by diffracting it off a crystal.

Consider a rotating copper anode operated at 6 kW power (30 kV, 200 ma). The flux from a copper anode, emitted isotropically is expressed as

$$F_{Cu} = 2.3 * 10^{-5} \frac{photons}{electron} * I * (E - E_0)^{1.63} \quad \dots\dots\dots\dots\dots\dots\dots\dots \quad (7)$$

Where E_0 is the energy of the characteristic line being considered and E is the maximum energy in the beam i.e the kVp and I is the tube current.

The flux after the lens is $F_{lens} = F_{Cu} * \frac{\Omega_{optic}}{\Omega} * T_{optic}$, where Ω_{optic}, Ω and T_{optic} represent the solid angle subtended by the optic entrance at the source, the total solid angle of emission (2π) and the transmission of the optic respectively.

Operating the source at 30 kVp and 200 ma gives an integrated count rate of $1.6 * 10^{11}$ photons/sec after the collimating prototype II.

The reflection efficiency of a diffracting crystal depends upon its angular bandwidth. This calculation is based on a Silicon crystal with a bandwidth of 0.02 mrad.

The output divergence of each polycapillary channel is less than twice the critical angle. The output angular divergence from a polycapillary fiber is fit with a gaussian with full width at half maximum (FWHM) of 2.25 mrad. The fraction of photons that would lie within the angular acceptance angle α, of a crystal is given by

$$f(\alpha) = \frac{1}{\sigma\sqrt{\pi}} \int_{-\alpha}^{\alpha} e^{-\left(\frac{\theta}{\sigma}\right)^2} d\theta, \text{ where } \sigma = \frac{FWHM}{2\sqrt{\ln 2}}.$$ With α= 0.02 mrad this fraction is

1.4 %.

The percentage of photons reflected by the crystal is obtained by multiplying the angular fraction $f(\alpha)$ by the fraction of photons emitted in the required energy range, $n(\Delta E)$ and the efficiency of reflection which is almost unity in this case.

The energy bandwidth for Bragg reflection is $\Delta E = \frac{\Delta\theta}{\theta} * E$ where θ is the bragg angle for the (400) reflection from silicon. The energy band width is about 0.3 eV, which is about one twentieth the width of a characteristic emission line from a tube source. For a copper target with tube potential of 30 kV, approximately 20 % of the emission lies in the K α line. This means about 1 % of the emission in the 0.3 eV portion of the bandwidth, $n(\Delta E) = 0.01$.

The integrated count rate after the crystal is then

$$F_{crystal} = F_{lens} * f(\alpha) * n(\Delta E)$$

or $F_{crystal} = 2.25 * 10^7$ photons / sec.

The flux obtained could be increased by increasing the tube loading and also by increasing the angular acceptance of the crystal. Mosaic crystals are considered good candidates for monochromator design due to their higher integrated reflectivities[17].(The calculation is for a silicon crystal with an acceptance width of 0.02 mrad. Highly oriented pyrolytic graphite for instance has a bandwidth of 5 mrad and by reflecting photons incident over this larger angular range would yield a higher reflected beam intensity).

A angular bandwidth of 0.5 mrad for instance would give f(α) = 39 % and this would give a reflected beam count rate of $3.1*10^9 \dfrac{photons}{sec}$.

The calculation demonstrates that sufficient monochromatic beam intensity could be obtained from a combination of rotating anode sources which can typically operate at 18 kW power and high mosaicity crystals.

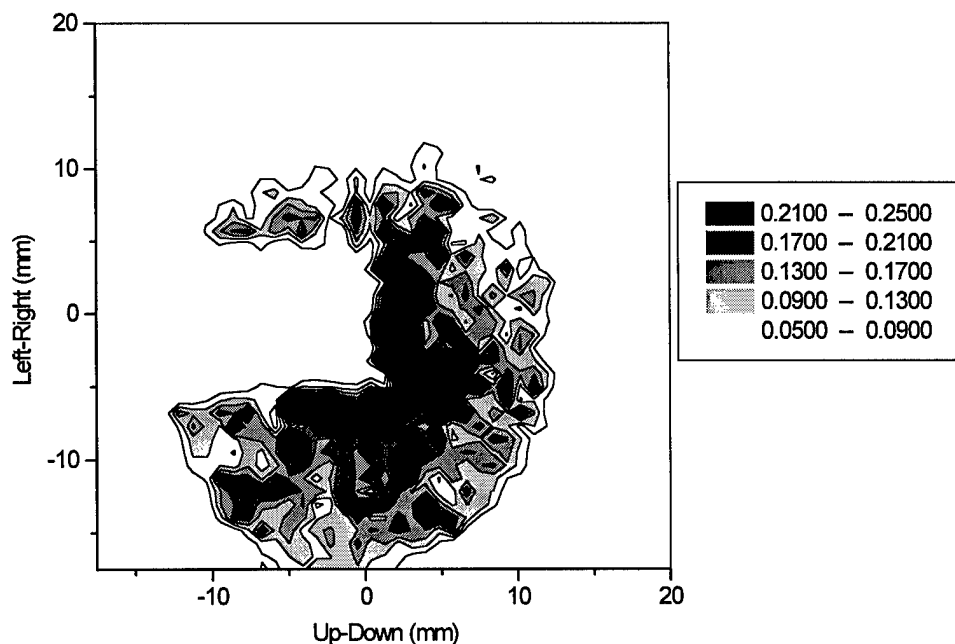## 2.3 Uniformity scan of output cross-section of prototype optic I

Fig 9: Output Intensity distribution from the prototype collimating optic I in the mammographic energy range 17-20 keV.

A 650 μm pinhole was scanned two-dimensionally across the output of the optic with scan step sizes of 750 μm. Fig 9 shows the results of this uniformity scan, which is consistent with the image in figure 3. The position of the lead block is clearly visible and blocks off a significant portion of the centrally located straight fibers that usually transmit very well. The prototype I largely presents a non-uniform output intensity profile. This optic was designed for 8 keV radiation and is too highly curved to work well at 20 keV.The prototype collimating type II transmits much higher in the energy range of interest for mammography and also has demonstrated a superior output uniformity. Details of this optic are presented in table II.

Section III
Linear Tapered Magnifying Scatter-Rejection Optics

Two prototype linearly tapered optics were measured for performance characterization in connection to future work in magnification, scatter rejection and contrast. These optics, unlike the collimating optics of section II would be used as post-patient "grids". Table II lays down the dimensions and the performances of these optics.

Table II.

Prototype Taper I	Prototype taper II
Profile : Linear	Profile : linear
Input diameter: 2 mm.	Input diameter : 1.9 mm
Output diameter : 4 mm	Output diameter : 3.82 mm
Input channel diameter : 5 μm	Input channel diameter : 4.9 μm
Output channel diameter : 10 μm	Output channel diameter : 9.8 μm
Optic length : 320 mm	Optic length : 350 mm
Transmission efficiency @ Mo K lines = 5 – 7 %.	Transmission efficiency @ Mo K lines: 9 – 12 %.
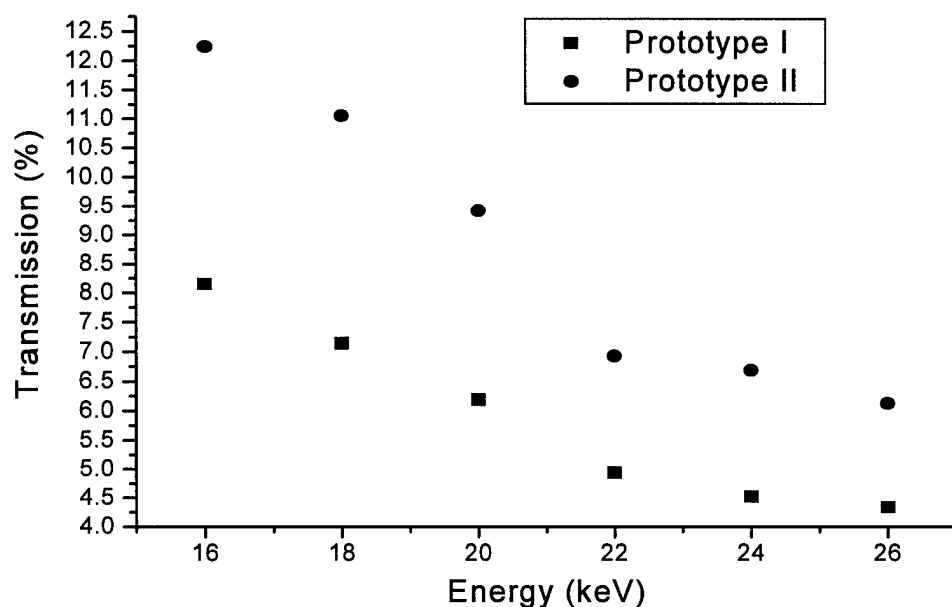
Fig 10: A comparison of transmissions of the linear two tapered prototypes.

Figure 10 compares the transmissions of these prototypes as a function of energy. An understanding of the poor transmission performance of prototype taper I was sought by snapping the optic into two parts, here onwards referred to as optic A and optic B respectively. Optic A is the longer piece (22 cms long) and whose output end formed the output end of the original optic. Optic B formed the shorter piece (10 cms long) whose input end formed the input end of the original optic.

The transmissions of Optic A and Optic B as a function of energy are plotted in figure 11.
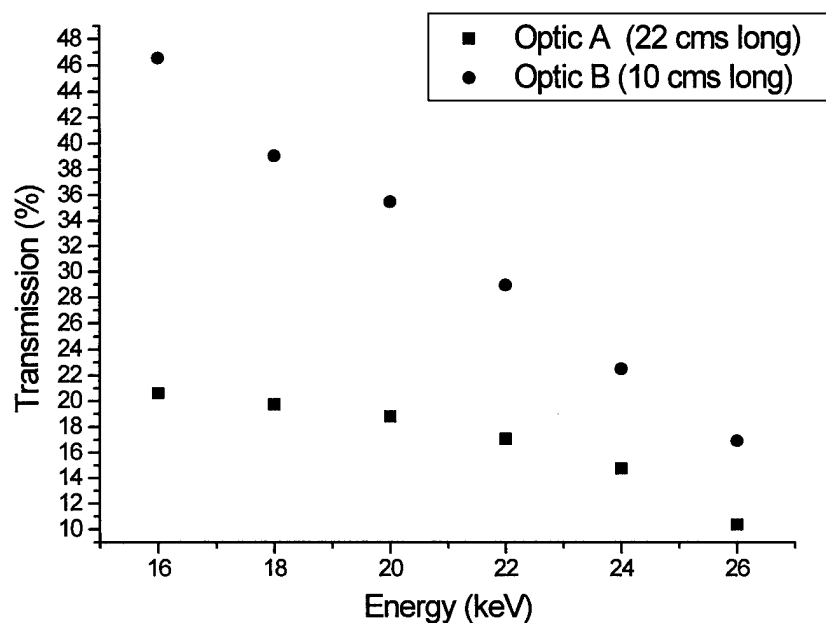
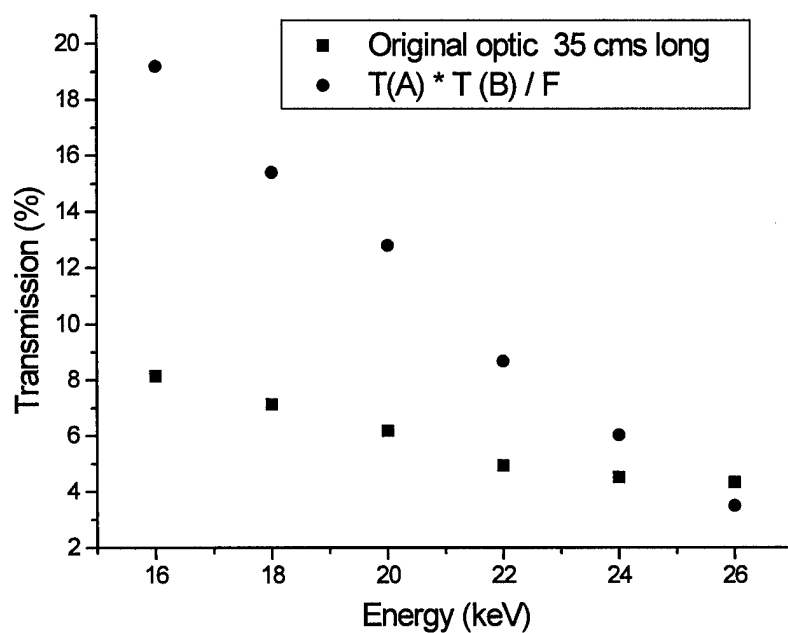*Fig 11: Individual transmissions of the two pieces A and B that made up linear prototype I.*

Fig 12: A comparison of the transmission of the original prototype I with the product of the transmissions of optics A and B, where T(A), T(B) and F represent
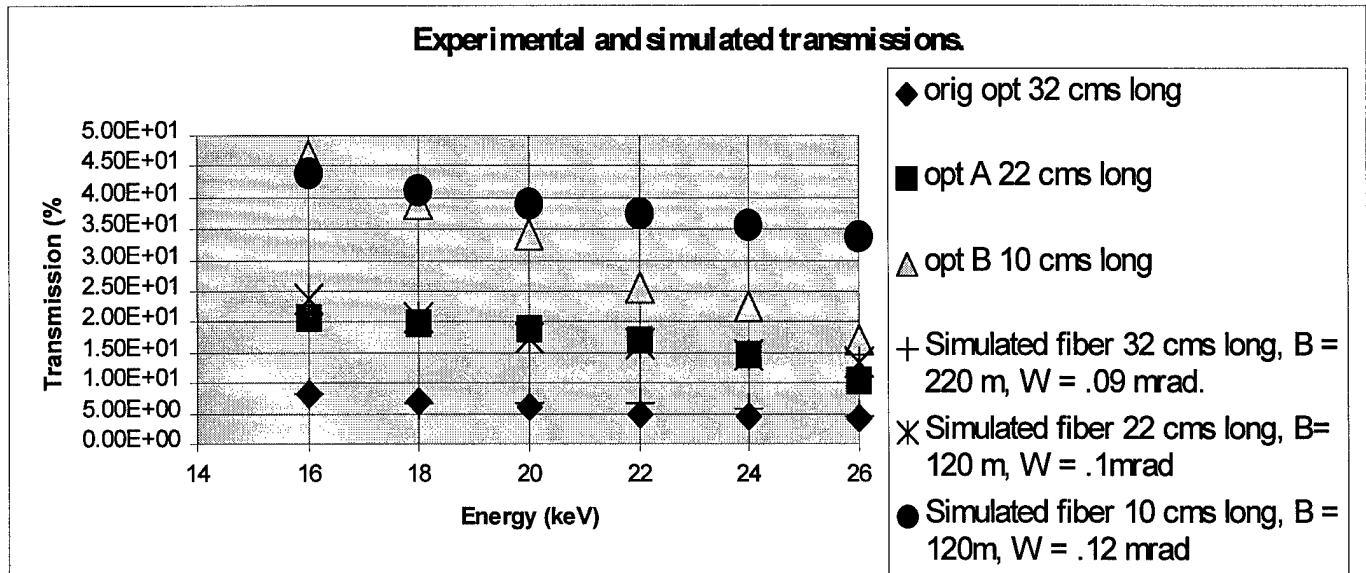
the transmission of optic A, transmission of optic B and the fractional open area of the optic respectively.

Both Optic A and optic B transmit much higher than the single optic that they constituted before being snapped. This is easy to understand as the transmission depends on the length of the optic, i.e. $T = F R^m$, where R is the reflectivity of the channels and depends on the incident angle as shown in fig 1 and m is the number of reflections the individual photons undergo between being incident on the input end and emerging from the output end of the optic. F is the fractional open area, which is the part of the input cross-section that is open, i.e, not blocked by the walls separating the channels.

Fig 12 illustrates the difference between the transmissions of the unsnapped optic and the product of the transmissions of optic A and optic B divided by the fractional open area of the optic, which was close to 50 % (The transmission of the optic is a product of the fractional open area and the reflectivity of the channels that transport the X-ray photons). This was understood to have been caused due to the following reason.

The second optic,Optic A now has a source to optic distance longer than that of the original optic. This results in smaller incident angles, thereby increasing the reflectivity. This leads to higher transmission values for optic A by itself than for when it follows optic B.

Simulations[18] were tried for straight fibers with channel sizes fiber dimensions matching that of the optic and these generally point to a combination of waviness and bending[19] that causes the transmissions of these optics to drop off rapidly at higher energies. Figure 13 shows the match between experimental results and simulations.

Experimental and simulated transmissions.

Legend
◆ orig opt 32 cms long
■ opt A 22 cms long
△ opt B 10 cms long
+ Simulated fiber 32 cms long, B = 220 m, W = .09 mrad.
✕ Simulated fiber 22 cms long, B= 120 m, W = .1mrad
● Simulated fiber 10 cms long, B = 120m, W = .12 mrad

Fig 13: Simulations carried out on straight fibers yield information on the waviness and bending of the fibers used in the manufacture of this prototype.W is the random tilt angle of the channel walls and B is the radius of curvature of the nominally straight fiber.

Bending has dimensions much larger than the wavelength being used and arises due to profile deformities. Waviness has smaller dimensions and arises due to the local tilting of the channel walls.

These simulations assume a straight fiber with no taper. A better understanding of these problems shall be acquired after the Monte Carlo simulation code that is being developed to characterize the performance of linear tapered optics becomes available.

3.1 Source scans of prototype linear taper II.

Source scans, measurements of lens transmission as the source is moved off axis, are shown in figures 14 a) and b), for various source-optic distances and photon energies respectively. Figure 14 a) determines the focal point of this optic

at 31 cms. The source scans are noticeably wider at distances longer or shorter than the focal distance. These scans demonstrate the excellent ability of these optics to efficiently reject off-axis radiation, a property highly desired in anti-scatter grids. The narrower scan widths at higher energies are due to the smaller critical angle for total reflection at higher energies.
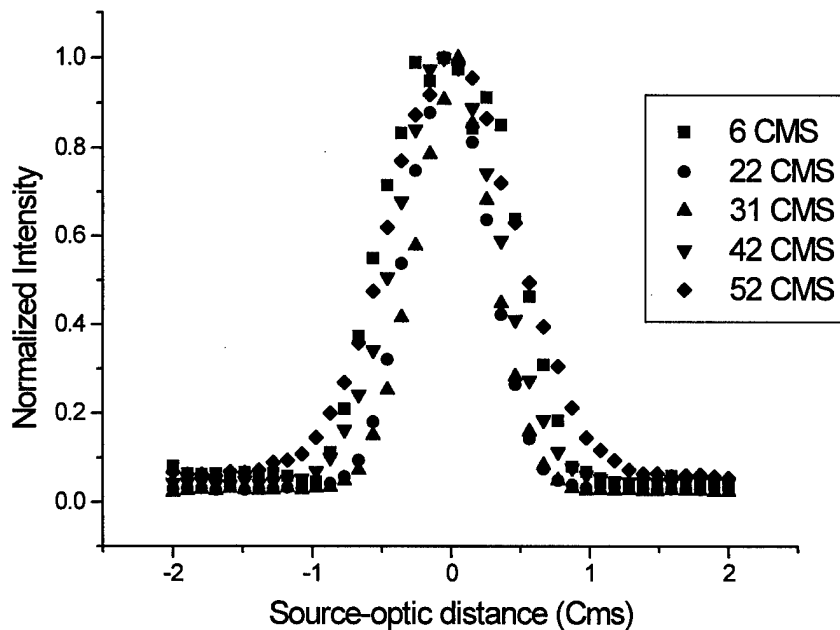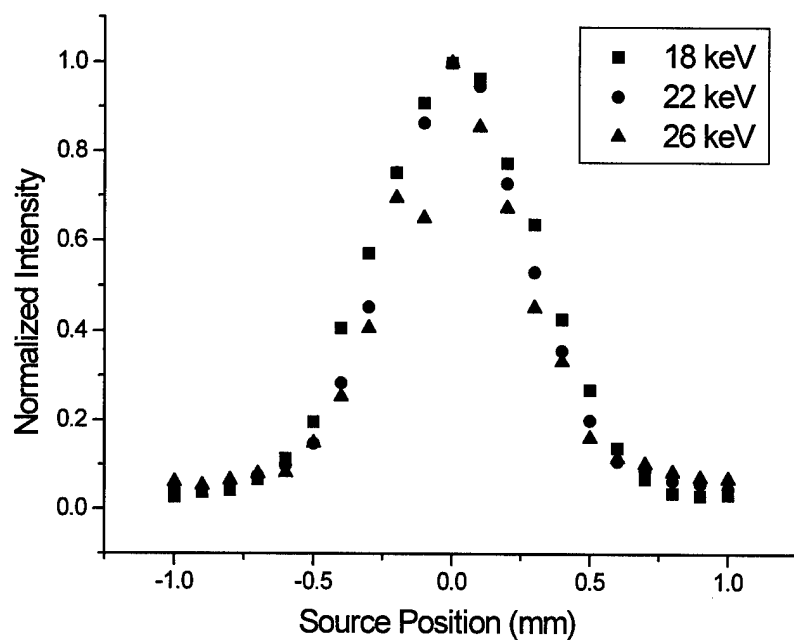

Fig14a) Source scans as a function of the source-lens distance.

.Fig 14 b) Source scan at the focal plane as a function of energy.

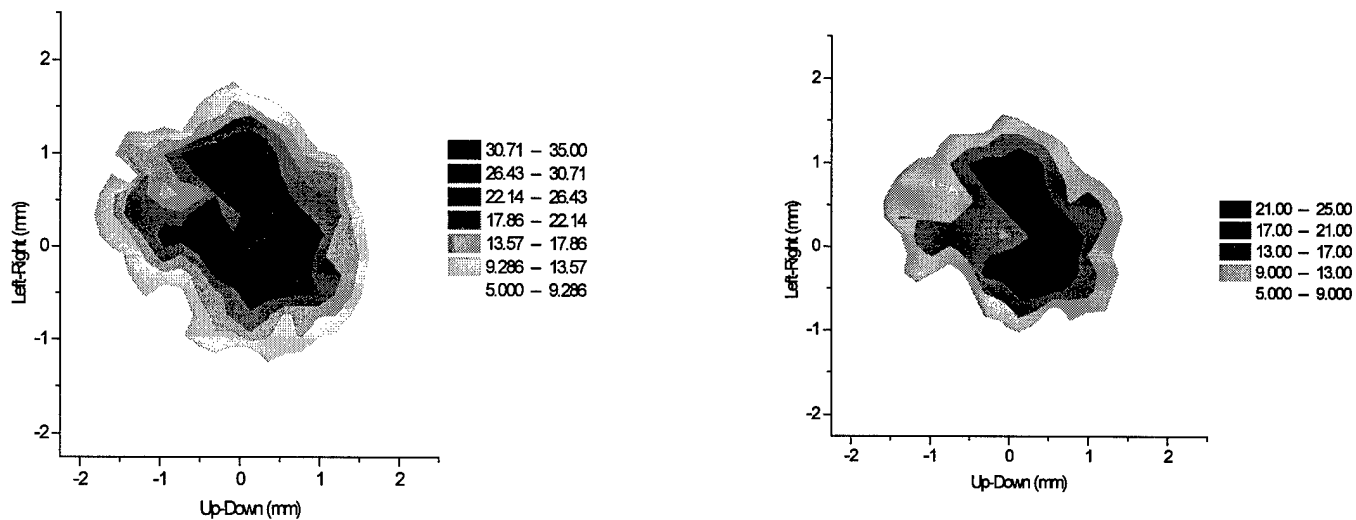## 3.2 Transmission Uniformities of Prototype linear taper II.

Fig 15 a) : Transmission uniformity at 14 keV (left) and 18 keV (right).
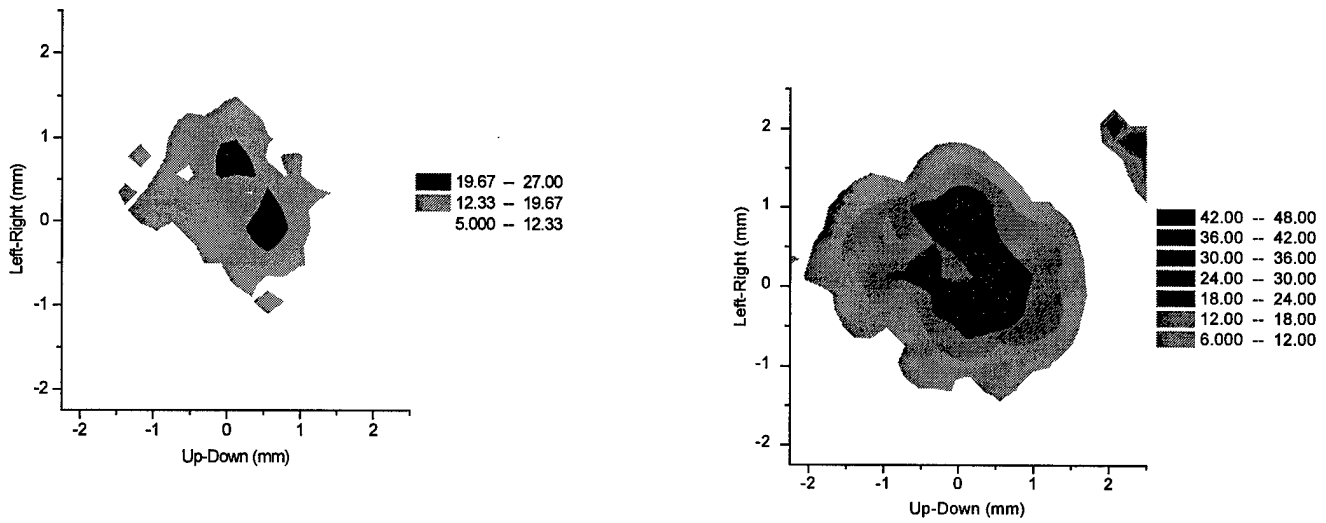
Fig 15b) Transmission uniformity at 22 keV (left) and the whole spectrum (right) (kVp = 26 kV)

Fig 15a) and fig 15b) are contour maps derived from a uniformity scan carried out at the output of the prototype linear taper II and yield information on the performance of localized regions of the optic. The central core of the optic transmits well essentially due to the straight profile of these fibers, but as we move away from this region, bending and waviness again appear. The cross-section that transmits is noticeably smaller at higher energies. This is because achieving a good transmission efficiency at higher energies requires the condition[20]

$$R_{Cr} \geq \frac{2d}{\theta_{Cr}^{2}(E)} \quad \cdots\cdots\cdots\cdots\cdots\cdots\cdots\cdots\cdots\cdots\cdots\cdots\cdots\cdots\cdots\cdots\cdots\cdots \quad (8)$$

to be satisfied. Here R_{Cr} is the radius of curvature of the fiber, d is the channel diameter and θ_{Cr} is the critical angle for total reflection. For borosilicate glass, the critical angle is given in milliradians by θ_{Cr} = 32 / E (keV). What equation (8) physically demands is small channel diameters and an absence of sharp bends, in order to transport high energy photons efficiently.

Results of simulations with the new code for these optics are awaited to be fed back into future manufacturing designs.

3.3 Scatter Fraction Measurements
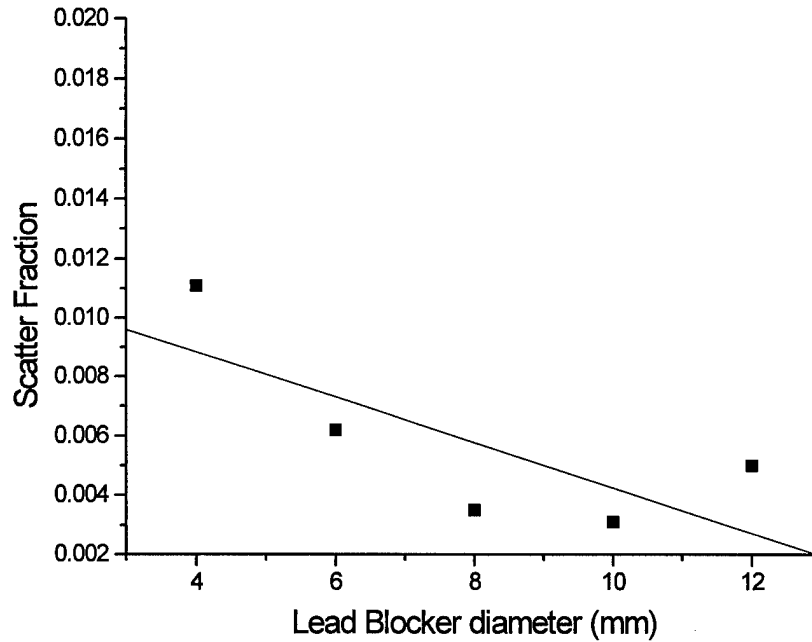
Fig 16: Scatter fraction measurement using the central straight fibers in prototype collimating optic II. These fibers are highly uniform in their performance.

An indicator of the potential of x-ray capillary optics as efficient scatter rejection devices for imaging purposes is demonstrated by the scatter fraction measurements shown in fig 16. The central core of the prototype collimating optic II which comprises of straight fibers that transmit well and uniformly was used for this measurement.

A lucite phantom was used before the optic and lead blocks of different dimensions were used to block parts of this phantom. The beam intensity right behind the lead blocker gives I_s, the scattered beam intensity. The beam intensity besides the blocker gives $I_s + I_p$, where I_p is the primary intensity.

Scatter fraction is then defined as $\dfrac{I_s}{I_s + I_p}$. The above measurement indicates a

scatter fraction of close to 1 %. Measurements are ongoing to compare this
result, for the no optic case and with an air gap.

Section IV
Conclusions

While prototype Collimating optic II has yielded higher transmission values and a
better output uniformity profile at mammographic energies, a smaller focal length
is desired for this optic to make better use of the source. This shall also provide
for greater flux at the output of this X-ray collimating device.

Measurements on linear tapered prototypes have revealed lots of information
that shall be beneficial in appropriately designing an optic for magnification,
scatter fraction and contrast measurements.

Future work

Measurements are ongoing and shall continue on recently manufactured linear
prototypes. Contrast detail phantoms used with the optic shall provide contrast
and scatter fraction information quantitatively. Prototype tapers that have
demonstrated superior performance in the measurements reported here shall be
put together to form a bulk optic.

Monochromatic imaging holds a lot of promise in connection to increased
resolution, enhanced contrast and reduced dose to the patient. The feasibility
analysis presented here shall be complemented with detailed experimental work.

Bibliography

[1] Bruce H.Hasegawa, The Physics of Medical Imaging (Medical physics publishing company, Nov 1991.

[2] David Kruger et al, "Imaging characteristics of x-ray capillary optics in digital mammography", Medical Physics. 23, 187-196 (1996).

[3] Physics Today, November 1997.

[4] Wei Zhao and John A. Rowlands, " A large area solid state detector for radiology using amorphous selenium", SPIE vol. 1651 Medical imaging vI: Instrumentation (1992).

[5] H.H. Rossi and A M. Kellerer, "Roentgen", Radiation research, 144, 124-128 (1995).

[6] C.A. MacDonald et al, " Quantitative measurements of the performance of Capillary x-ray optics", in Multilayer and Grazing incidence x-ray/EUV optics II, edited R.B. Hoover and A.Walker, SPIE Proc. Vol. 2011, (1993).

[7] J.B. Ullrich, V.Kovantsev and C.A. MacDonald, " Measurements of Polycapillary x-ray optics," J.Appl. Phys. 74 (10), 5933-5939 (1993).

[8] J.D. Jackson, "Classical Electrodynamics", John Wiley & sons, New York.

[9] A.H. Compton and S.K. Allison, " X-rays in theory and experiment " D. Van Nostrand company, Inc, New York.

[10] " Studies of Monolithic Capillary optics for small sample crystallography " Johannes ullrich, A Ph.D dissertation, Department of Physics, state University Of New York At Albany.

[11] F. Arfelli, A.Bravin, G.Barbielinni et al, "Digital mammography with synchrotron radiation" Rev.Sci.Instr., Vol 66, No.2, Febraury 1995.

[12] J.M. Boone and J. A Seibert, Med. Phys. 21 (1994) 1853.

[13] R.J.Jennings, P.W.Quinn et al, SPIE Proc. 1896 (1993) 259.

[14] C.A. MacDonald and W.M. Gibson " Medical Applications of Polycapillary x-ray optics" " SPIE vol. 2519, July 1995.

[15] E. Burattini, M. Gambaccini et al, Rev. Sci. Instr. 63 (1992) 638.

[16] E. Burratini, M. Gambaccini et.al, Euro . Rad. 4 (1994) 464.

[17] A.K.Freund, Nuclear.Instr.Meth.A 266 (1988) 461.

[18] Q.F.Xiao, J.C.Kimball et al, " Numerical Simulations for Capillary-based X-ray optics" in X-ray detector physics and applications, R.B.Hoover ed, SPIE vol.1736,pp227-238,1992.

[19] Lei Wang, B.K.Rath, W.M.Gibson, J.C.Kimball, C.A.MacDonald, "Performance study of Polycapillary optic performance for hard x-rays", Journal of Applied Physics, 80 (7),pp.3628-3638, October 1, 1996.

[20] C.A.MacDonald "Applications and Measurements of Polycapillary X-ray optics", Journal of X-ray science and Technology 6, 32-47 (1996).